JOURNAL OF SPACECRAFT AND ROCKETS
Vol. 29, No. 2, March-April 1992

Computation of Near-Wake, Aerobrake Flowfields

Peter A. Gnoffo,* Joseph M. Price,† and Robert D. Braun‡
NASA Langley Research Center, Hampton, Virginia 23665

Simulations of the near-wake flowfield behind three aerobrakes have been implemented with Program LAURA, an algorithm for obtaining the numerical solution to the governing equations for three-dimensional, viscous, hypersonic flows in chemical and thermal nonequilibrium. Emphasis is placed on understanding the conditions that are likely to cause the shear layer to impinge on a payload positioned behind the aerobrake. A linear relationship between shear-layer deflection angle and angle of attack (or lift-to-drag ratio) has been identified in several ground-based tests. A similar relation appears in the numerical simulations, though there is some evidence that deflection angles may increase somewhat due to the effects of gas chemistry. Shear-layer impingement can raise local heating levels a factor of 10 higher than levels present without impingement.

Nomenclature

C_D = coefficient of drag
C_L = coefficient of lift
D = base diameter, m
H = total enthalpy, J/kg
h = altitude, km
L/D = lift-to-drag ratio
M = Mach number
N_e = electron number density, 1/cm^3
$N_{Re_{\infty,D}}$ = Reynolds number based on freestream conditions and base diameter
$N_{Re_{2,D}}$ = Reynolds number based on postnormal shock conditions and base diameter
$N_{Re_{\text{cell}}}$ = Reynolds number based on mesh height and local sound speed
p = pressure, N/m^2
q = heating rate, W/cm^2
R_N = aerobrake nose radius, m
R_S = aerobrake shoulder radius, m
T = translational-rotational temperature, K
T_V = vibrational-electronic temperature, K
V = velocity, m/s
x, y, z = aerobrake coordinates, in.
α = angle of attack referenced to base plane normal, deg
β = aerobrake cone angle, deg
δ = rake angle of base plane relative to cone axis, deg
ϵ = eccentricity of aerobrake nose
θ = shear-layer deflection angle referenced to base plane normal, deg
ρ = density, kg/m^3

Subscripts

∞ = conditions in freestream
2 = conditions behind normal shock

Introduction

WITHIN the context of the Space Exploration Initiative, there are three potential applications for aerobraking: 1) Mars arrival, 2) Earth return from Mars, and 3) Earth return from the Moon. From a performance standpoint, aerobraking upon Mars arrival yields the most significant savings. In a typical mission scenario, one or two relatively large, blunt aerobrakes are utilized to provide the deceleration required to achieve Mars orbit. These aerobrakes, which are generally on the order of 25–40 m in base diameter, are utilized to shield a Mars payload, which can be defined as a cylindrical volume approximately 20 m in diameter and 25 m in length.[1] For Earth return from Mars, current initial exploration scenarios utilize a small (5-m base diameter) capsule-type vehicle, and wake flow impingement on a payload is not an issue. For Earth return from the Moon, present concepts are characterized by a single, blunt aerobrake 15 m in base diameter that shields a cylindrically shaped payload volume of approximately 7.5 m in diameter and 9 m in length.

The payload components are packaged behind an aerobrake according to two criteria. The first criterion is that the vehicle center-of-gravity constraints must be satisfied such that stable flight is achieved at the proper lift-to-drag (L/D) ratio to compensate for atmospheric, aerodynamic, and initial-state uncertainties. Payload placement is the only means to satisfy these center-of-gravity requirements because the low L/D vehicles currently under consideration do not have aerodynamic control surfaces, nor do they rely on thrusting during the atmospheric pass. The second criterion is that, in an effort to minimize mass, the present concepts (with the exception of the Earth-return capsule) do not incorporate an aft structure or thermal protection system; consequently, the payload must be positioned in a relatively quiescent region of the near wake to minimize thermal and aerodynamic loads.

Numerical simulation of this near-wake flowfield is a formidable task. The near-wake domain is topologically challenging with regard to the ordering and distribution of mesh points. The flowfields will not be axisymmetric, and the wake recirculation region is quite complex. Resolution of the shear layer and wake recompression region, which are critical drivers of the flow in this region, requires some combination of grid adaption and multidomain data structure.

With typical perigees on the order of 70–80 km for Earth return from the Moon, densities and density gradients are predicted in the near wake that yield local Knudsen numbers near the separation point of order 0.1.[2] At higher altitudes, the upper limit of Knudsen number will increase and compromise the applicability of continuum analyses.

The importance of unsteady flow effects in the wake has not yet been quantified. Predictions of convective heating on a

---

Presented as Paper 91-1371 at the AIAA 26th Thermophysics Conference, Honolulu, HI, June 24–26, 1991; received Aug. 19, 1991; revision received Dec. 2, 1991; accepted for publication Dec. 6, 1991.

*Aerospace Engineer, Aerothermodynamics Branch, Space Systems Division. Associate Fellow AIAA.

†Aerospace Engineer, Aerothermodynamics Branch, Space Systems Division.

‡Aerospace Enginer, Vehicle Analysis Branch, Space Systems Division. Member AIAA.

sting behind an aerobrake for conditions in the Langley 31-in. Mach 10 facility were in good agreement with experimental data using only a laminar, steady flow model.[2] However, shadowgraphs from the Ames ballistic range of the near wake behind an aerobrake show some waviness in the wake neck and recompression shock that are indicative of flow unsteadiness. Any critical analysis of flow unsteadiness must sacrifice the simplifying assumption of planar symmetry so that all unsteady modes are allowed.

Finally, density and energy distributions in the near wake are strong functions of thermochemical nonequilibrium effects. Most of the energy exchange models currently in use are derived from experimental data in compression zones behind normal shocks. The situation is reversed for the severe expansion into the wake, and the applicability of many current models is again compromised.

The available experimental data are not sufficient to validate present computational models, though there is much that should be exploited to calibrate codes at off-design conditions.[2] Ground-based and flight programs[3] for obtaining experimental data applicable to these regimes must be given highest priority if aerobrake designs are to proceed without excessive safety factors that might ultimately defeat the viability of the concept. Computational tools must be used for the preliminary design of experiments to ascertain what aspects of the modeling are most challenging and to assess what kind of measurements will validate said models.

Computational tools may also be used for the preliminary design and evaluation of various aerobrake concepts; however, the designers must be aware of the aforementioned uncertainties in present analyses. Parameter studies and grid refinement studies may be used to bound the sensitivity of predicted quantities to some model unknowns. Such studies have been in progress for the past three years with regard to the design of the Aeroassist Flight Experiment (AFE).[2,4,5] The purpose of the present paper is to document the studies completed to date for the AFE, with emphasis on the description of the near-wake and free-shear layer impingement flows and to further explore the issue of wake closure for a proposed lunar return aerobrake.

Numerical Approach

The Langley Aerothermodynamic Upwind Relaxation Algorithm (LAURA)[6,7] is applied to simulate flowfields surrounding the AFE aerobrake and carrier and a proposed lunar return vehicle at selected trajectory points. Vehicle geometries are summarized in Table 1. The trajectory points studied for each vehicle are presented in Table 2. The case labeled "afe-1" corresponds to one of the earliest points on the AFE trajectory at which continuum analyses are credible in the shock layer over the aerobrake. The case labeled "afe-4" corresponds to the peak heating point on a nominal trajectory for return from geosynchronous Earth orbit. The case labeled "lunar" corresponds to the peak heating point on a nominal trajectory for return from the Moon. Computed aerodynamic coefficients for these cases at several angles of attack are recorded in Table 3.

Table 1 Vehicle parameters

Case	D	R_N	R_S	β	δ	ϵ
afe	4.2469	3.8608	0.3861	60	73	2.0
lunar-a	7.3152	3.0480	0.3048	70	90	1.0
lunar-b	7.3152	3.0480	0.6096	70	90	1.0
lunar-c	13.7160	3.0480	0.3048	70	90	1.0

Table 2 Trajectory point parameters

Case	V_∞	ρ_∞	T_∞	$N_{Re_{\infty,D}}$	$N_{Re_{2,D}}$	h
afe-1	9863	5.682E-06	189	20,900	560	87
afe-4	9326	4.293E-05	200	143,000	5,600	75
lunar	9871	4.623E-05	210	269,000	9,600	75

Table 3 Aerodynamic parameters

Case	α	C_L	C_D	L/D
afe-1	17	0.366	1.37	0.267
afe-1	22	0.443	1.27	0.349
afe-4	12	0.302	1.43	0.211
afe-4	17	0.376	1.33	0.283
afe-4	22	0.429	1.22	0.352
lunar-a	0	0.000	1.65	0.000
lunar-a	10	0.232	1.53	0.152
lunar-b	10	0.206	1.45	0.142
lunar-c	10	0.239	1.58	0.151

LAURA is an upwind-biased, point-implicit relaxation algorithm for obtaining the numerical solution to the governing equations for three-dimensional, viscous, hypersonic flows in chemical and thermal nonequilibrium. The algorithm is derived using a finite-volume formulation in which the inviscid components of flux across cell walls are described with Roe's averaging[8] and Harten's entropy fix[9] with second-order corrections based on Yee's symmetric total variation diminishing scheme.[10,11] The modeled system includes continuity equations for 11 species, 3 momentum equations, and 2 energy equations describing the conservation of vibrational-electronic and total energies. Species 1-5 are the neutral components of air consisting of N, O, N_2, O_2, and NO. Species 6-10 are the ions corresponding to species 1-5, in which one electron has been removed. Species 11 is the free electrons. The vibrational and electronic energies of all species are assumed to be in equilibrium at temperature T_V. The translational and rotational energies of all species are assumed to be in equilibrium at temperature T. Justifications for these assumptions, which constitute a two-temperature model for thermal nonequilibrium, are discussed by Park.[12] No-slip and finite-rate wall catalytic boundary conditions[13] are used throughout. Aerobrake surface temperatures are held constant at 1750 K. Base surface and payload surface temperatures are held constant at 1000 K for the afe cases and at 1500 K for the lunar cases. Radiative energy transport is not included in the computations. (Radiative heating accounts for about 5% of the total, maximum heating for case afe-4 and about 80% of the total heating for case lunar-c.)

Lunar-Aerobrake Results

Three-Dimensional Flow—Forebody

A new approach has been taken in the definition of the lunar aerobrake that avoids the problems associated with the axis singularity in the stagnation region. This singularity may induce erratic behavior in the calculated heat transfer distribution. These problems were specifically addressed in Ref. 14 where it was noted that a localized grid restructuring does much to overcome the problem. This concept was extended to create a more uniform, singularity-free surface mesh as shown in Fig. 1. Some grid skewness is necessarily introduced in mapping the corners of the surface grid to the 45- and 135-deg rays at the edge of the circular shoulder as shown in Fig. 1b; however, extracted line plots and surface contour plots show little or no associated distortion. Note that cells that appear triangular in fact have four sides, of which two sides of opposite family run parallel to the base plane from the same surface point. A grid-generation package for general blunt bodies with circular shoulders derived from circular or elliptic cones has been coded to simplify the definition of singularity free grids. As an added benefit, the new grid structure provides enhanced circumferential distribution of cells that feed directly into the wake. All of the lunar aerobrake flows were generated with this new grid structure. (Some of the AFE forebody flows have been repeated on the new grids; however, the recomputation of the AFE wake flows with the new grid structure has not been completed.)

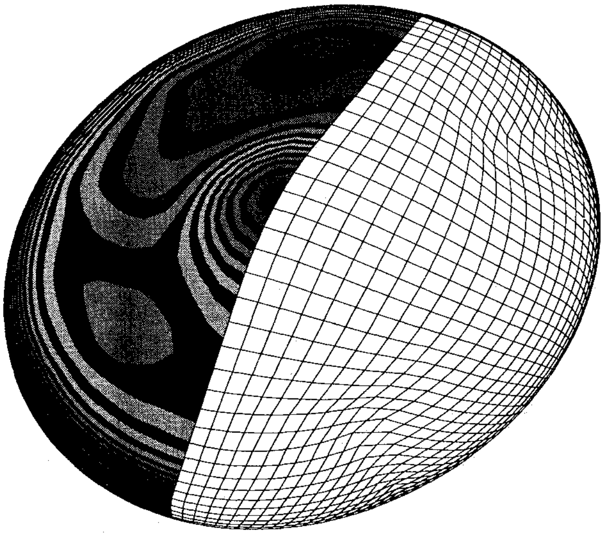

a) **Overview of mesh and heating**

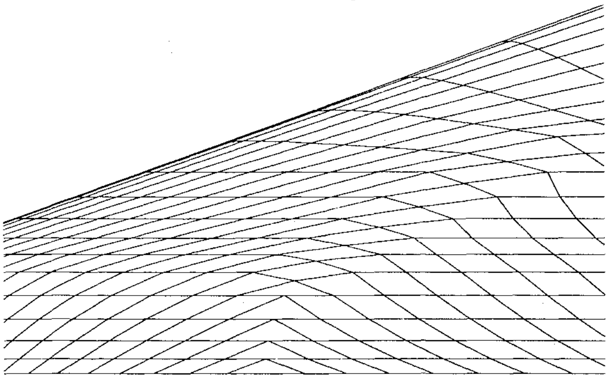

b) **Detail of mesh on the shoulder at a 45-deg ray**

Fig. 1 Surface mesh and heating contours over aerobrake for case lunar-a at $\alpha = 10$ deg.

Convective heating contours for case lunar-a at $\alpha = 10$ deg are also presented in Fig. 1. Heating distributions for cases lunar-a, lunar-b, and lunar-c along the plane of symmetry at $\alpha = 10$ deg are compared in Fig. 2. These distributions show none of the erratic behavior evidenced in earlier work associated with the coordinate singularity. The peak heating point for the lunar-a configuration occurs on the shoulder for $\alpha = 10$ deg. The larger shoulder radius of the lunar-b configuration reduces the peak shoulder heating (the reduction factor is slightly less than the square root of shoulder radii ratio) at the expense of lower values for C_L, C_D, and L/D. The larger base radius of the lunar-c configuration raises the effective radius of curvature of the stagnation point on this sonic corner body, thus reducing stagnation point heating relative to the two smaller bodies, even though they all have the same nose radius. The impact of the shoulder radius change on gross features of the wake flow is small, as will be discussed in a later section.

Three-Dimensional Flow—Wake

The outer boundaries of the wake computational domain in the symmetry plane are straight lines extrapolated from the last two points of the outer boundaries of the forebody grid. The forebody grid has been aligned with the captured bow shock but no alignment of the grid with the bow shock in the wake is attempted. An exit plane location is specified at a fixed z location several base diameters behind the base. An initial flowfield is calculated to establish the approximate positions of the free shear layer and wake core. Grid control points can be adjusted to enhance resolution of these structures. The inner wake grid is then reconfigured into a funnel-like shape in which the converging surface of the funnel extends from the aerobrake shoulder to the wake neck and the tubular extension of the funnel follows the wake core to the exit plane. A representative grid is shown in Fig. 3.

Pressure contours in Fig. 4 clearly show the recompression shocks surrounding the wake core, as defined by the streamlines in Fig. 5 for case lunar-a at $\alpha = 10$ deg. The recompression shocks are diffused somewhat because they are oblique to the grid aligned with the wake core. Better resolution requires application of a solution adaptive grid strategy as in Ref. 15. The subsonic flow domain in the wake, one measure of a relative quiescent zone for payload packaging, is shown in Fig. 6. The translational and vibrational temperature contours and electron number densities in the near wake are recorded in Figs. 7–9.

Axisymmetric Flow

A series of tests were performed for axisymmetric flows to assess the impact of various parameters on gross wake flow

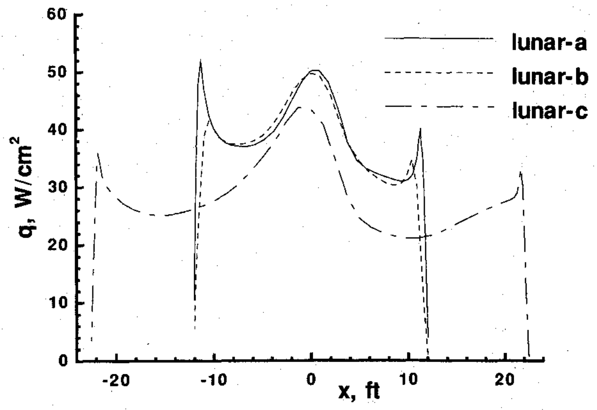

Fig. 2 Comparisons of heating distributions for configurations lunar-a, lunar-b, and lunar-c at $\alpha = 10$ deg.

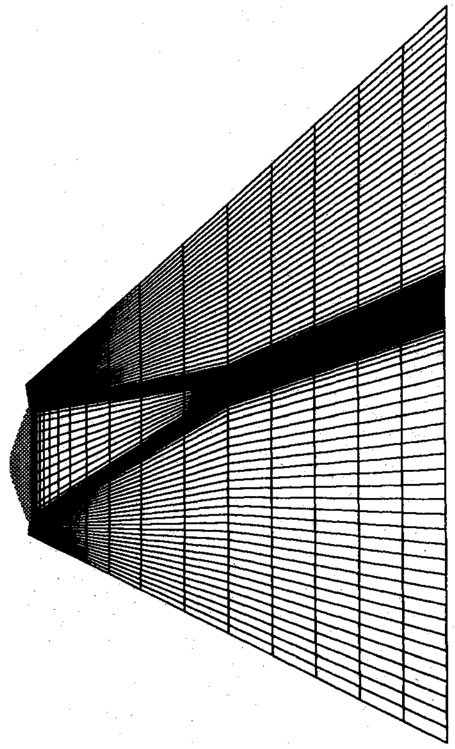

Fig. 3 Grid in symmetry plane of near wake behind lunar aerobrake lunar-a at $\alpha = 10$ deg.

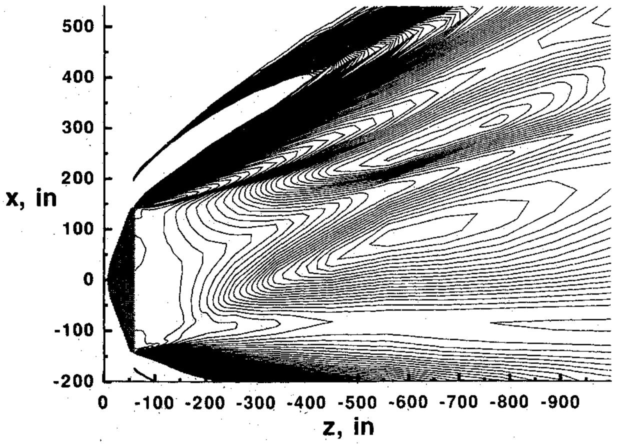

Fig. 4 Pressure contours in symmetry plane in near wake behind lunar aerobrake lunar-a at $\alpha = 10$ deg. Contour levels defined by $p/\rho_\infty V_\infty^2$ varying between 0 and 0.04 with 81 levels, inclusive.

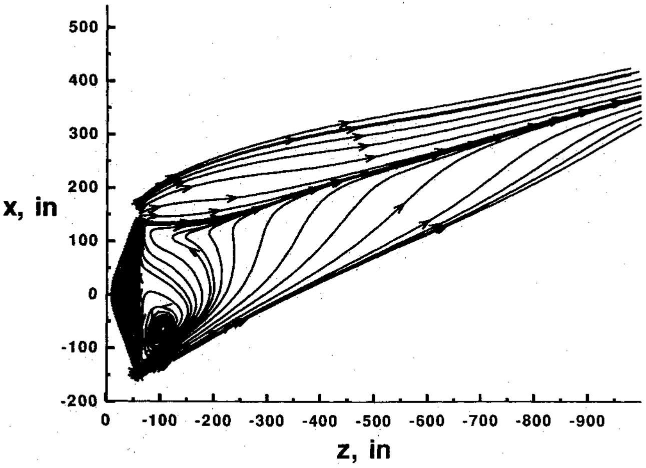

Fig. 5 Streamlines in symmetry plane in near wake behind lunar aerobrake lunar-a at $\alpha = 10$ deg.

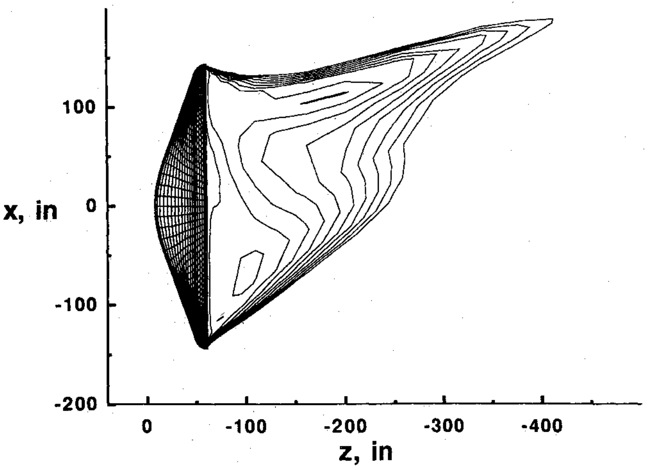

Fig. 6 Mach number contours in symmetry plane in near wake behind lunar aerobrake lunar-a at $\alpha = 10$ deg. Contour levels vary between 0 and 1.0 with 11 levels, inclusive.

character. The baseline model consisted of reacting flow using Park's reaction set,[6] constant wall temperature of 1500 K, full Navier-Stokes equations, and fixed inflow boundary conditions taken from the forebody solution. Variations on this modeling include frozen flow and flow using the Dunn and Kang reaction rate set,[6] reduced Navier-Stokes equations defined by the thin-layer approximation in all coordinate directions (cross derivatives omitted), base wall temperature changed to 1000 K, and fully coupled forebody and wake flow. All tests were conducted on the same grid and the residual norms of all solutions were taken to equivalent levels.

Space limitations preclude a comprehensive review of these parameter studies; however, it is encouraging to note that near-wake flow features were not significantly altered by these variations. The use of the full Navier-Stokes equations tended to delay separation somewhat from the thin-layer approxima-

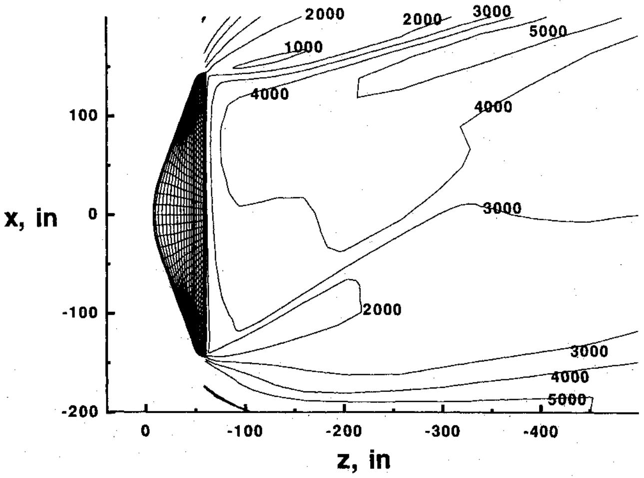

Fig. 7 Translational-rotational temperature T contours in symmetry plane in near wake behind lunar aerobrake lunar-a at $\alpha = 10$ deg.

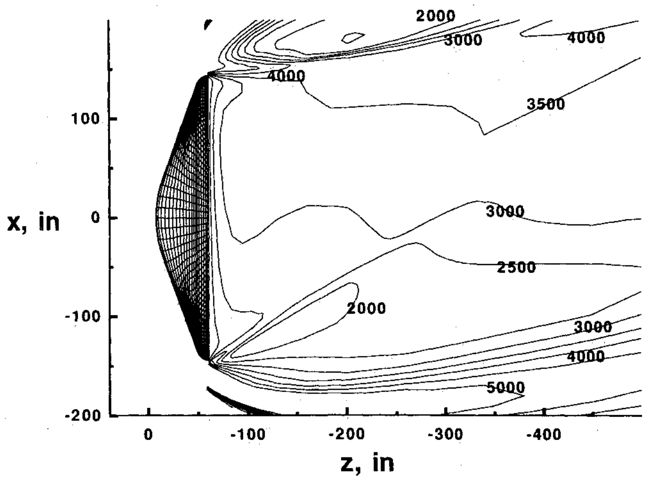

Fig. 8 Vibrational-electronic temperature T_V contours in symmetry plane in near wake behind lunar aerobrake lunar-a at $\alpha = 10$ deg.

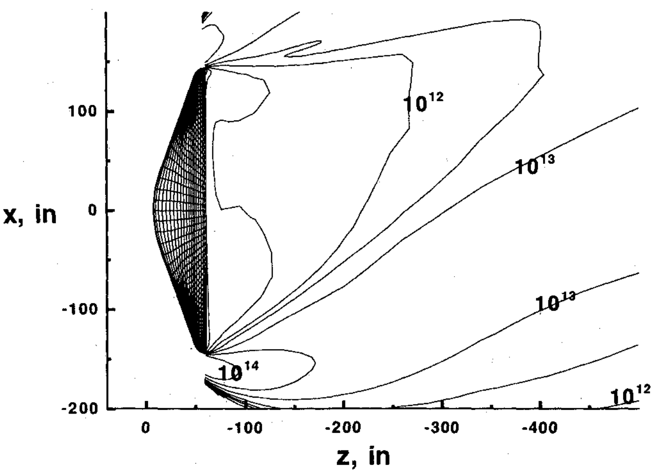

Fig. 9 Electron number density N_e contours in symmetry plane in near wake behind lunar aerobrake lunar-a at $\alpha = 10$ deg.

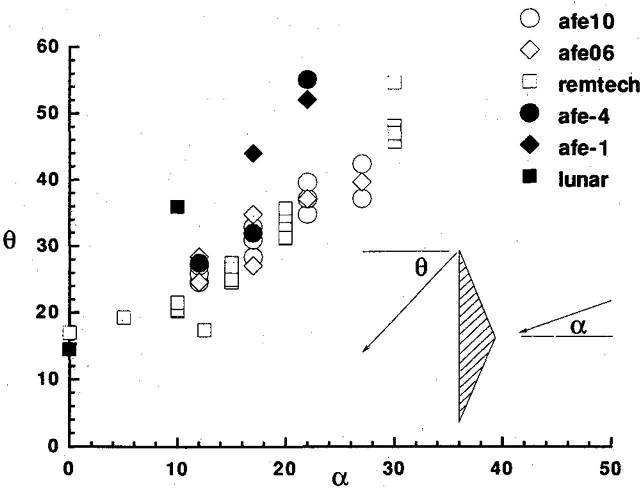

Fig. 10 Wind side shear layer deflection angles vs angle of attack. Open symbols derived from ground based experimental data. Closed symbols derived from calculated sonic line location behind aerobrakes at representative trajectory points.

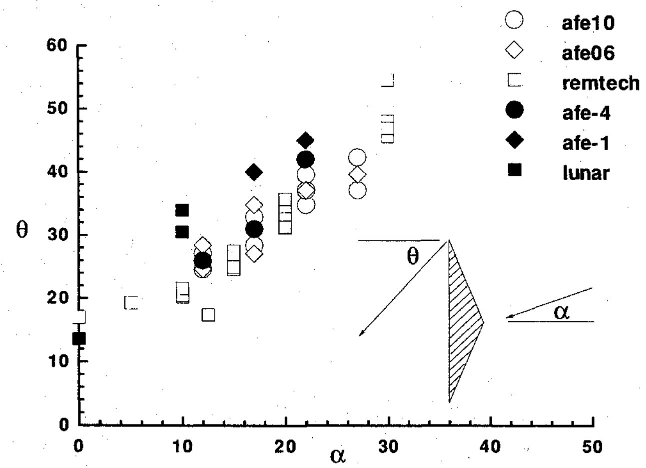

Fig. 11 Wind side shear layer deflection angles vs angle of attack. Open symbols derived from ground based experimental data. Closed symbols derived from calculated total enthalpy contour ($H/V_\infty^2 = 0.3$) behind aerobrakes at representative trajectory points.

tion causing a slightly larger deflection of the free shear layer (see the following section). The differing kinetic models caused some small changes in temperature contour placement, but the character and size of the recirculation zone was predominantly unchanged.

The most interesting feature of the axisymmetric wake flow is the presence of a very strong recompression core at the wake neck that drives the recirculating flow toward the base at a Mach number equal to 1.3. A shock is formed in front of the base, the flow stagnates at the axis of the base and then accelerates outward along the base to the free shear layer. This behavior has been observed in earlier work,[16,17] but always in a context that forced axisymmetric flow. This case was rerun on a three-dimensional grid (with symmetry plane), and perturbations were introduced at the inflow boundary to see if the "recirculation shock" solution was well posed. Again, no significant changes to the gross flow features were induced using either the three-dimensional grid or the inflow boundary perturbations.

Shear-Layer Deflection Angles

The location of the free-shear layer in the near wake roughly bounds the usable volume behind the aerobrake available for positioning payload. Shear-layer impingement causes high, localized convective heating rates with magnitudes dependent on the severity of the impingement angle and the payload effective radius at the impingement zone. Furthermore, if the payload extends through the shear layer, aerodynamic loads on it may significantly influence the aerodynamics of the complete vehicle.

Shear-layer deflection angle θ and angle of attack α are measured relative to a direction normal to the base plane of an aerobrake. A review of both experimental data and numerical simulations shows that the shear-layer deflection angle is largest on the wind side of the vehicle. Figures 10 and 11 present some of these results from ground-based experiments (open symbols) and numerical simulations of aerobrake flowfields in flight (closed symbols). Data labeled afe10 and afe06 are from test results[18] for an AFE model taken in the Langley 20-in. Mach 6 tunnel and the Langley 31-in. Mach 10 tunnel at Reynolds numbers $N_{Re_{\infty,D}}$ between 76,500 and 612,000 (normal shock values $N_{Re_{2,D}}$ between 6300 and 50,000). Data labeled "remtech" are for a family of blunt axisymmetric bodies tested[19] in the Langley 31-in. Mach 10 tunnel at Reynolds numbers $N_{Re_{\infty,D}}$ between 133,000 and 333,000 (normal shock values $N_{Re_{2,D}}$ between 11,000 and 27,000). The deflection angles were measured from a straight line drawn from the wind side base corner to the measured location of the flow attachment point on the payload/sting from oil flow patterns or to the peak heating point on the payload/sting as measured using phase change paints or heat transfer gauges. A linear trend is observed in the relation between α and θ in the experimental results (open symbols). A schlieren photograph at Mach 6 shows a shear-layer deflection angle that correlates well with

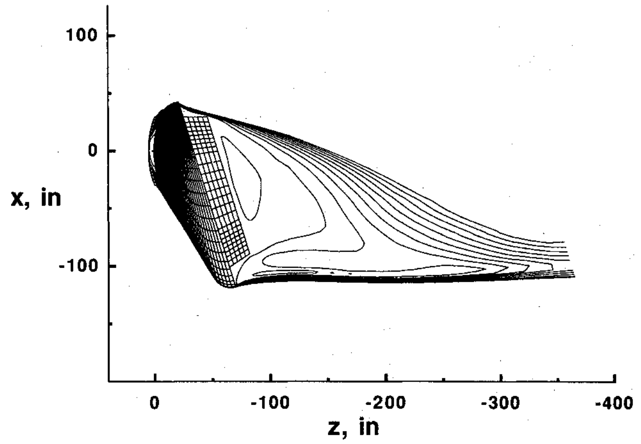

Fig. 12 Mach number contours for case afe-4 at $\alpha = 0$ deg. Contour lines vary between 0.0 and 1.0 with increment equal to 0.1.

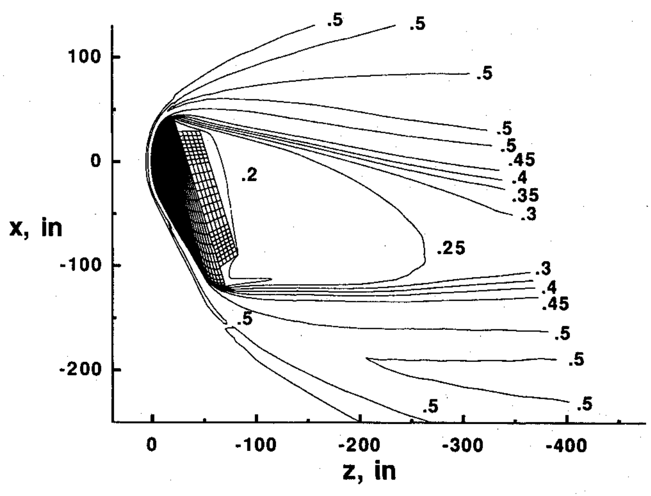

Fig. 13 Total enthalpy contours, H/V_∞^2, for case afe-4 at $\alpha = 0$ deg. Contour lines vary between 0.0 and 0.5 with increment equal to 0.05.

the linear trend.[18] No significant effects due to M_∞, $N_{Re_{\infty,D}}$, or vehicle geometry are observed in these ground-based tests.

Two measures of shear-layer deflection angle have been applied to the numerical simulations of wake flows in flight (closed symbols). Freestream conditions and other defining characteristics for simulation cases defined by afe-4, afe-1, and lunar have been defined previously in Tables 1 and 2. The sonic line location has been used in Fig. 10. A total enthalpy contour ($H/V_\infty^2 = 0.3$), approximately equal to 60% of the freestream total enthalpy, has been used in Fig. 11. The sonic line is initially embedded in the shear layer. Any payload contained within the sonic line should be shielded from potentially adverse shock/boundary-layer interactions. (The perturbing effect of a payload on the sonic line location in the wake has not yet been studied.) However, as the flow accelerates toward the wake core, the sonic line diverges from the shear layer. This behavior tends to increase the calculated value of θ as defined in this manner and consequently reduces the effective volume available for packaging payload. The total enthalpy defines the driving potential for heat transfer and tends to follow streamlines in the shear layer through the near wake. Therefore, it may be a better delimiter for usable volume behind the aerobrake. These relationships between sonic line, total enthalpy contours, and streamlines can be observed in Figs. 12–14.

The measure of θ based on total enthalpy is in better agreement with the ground-based data in Fig. 11, though in general there appears to be a slightly larger deflection at flight conditions, which may be a gas chemistry effect. If gas chemistry is an important parameter for evaluation of shear-layer deflection angles, then caution should be exercised before applying the results of Fig. 11 to Martian entry conditions.

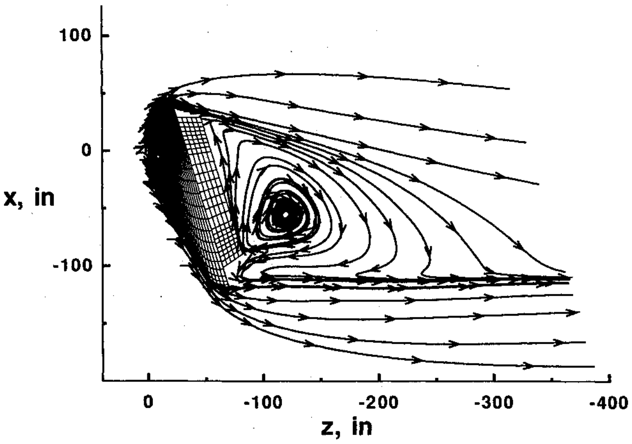

Fig. 14 Streamlines for case afe-4 at $\alpha = 0$ deg.

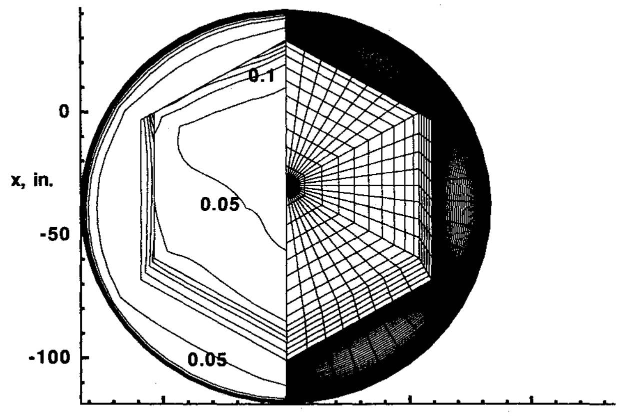

Fig. 15 Bottom view of heating contours q on AFE carrier for case afe-4 at $\alpha = 22$ deg.

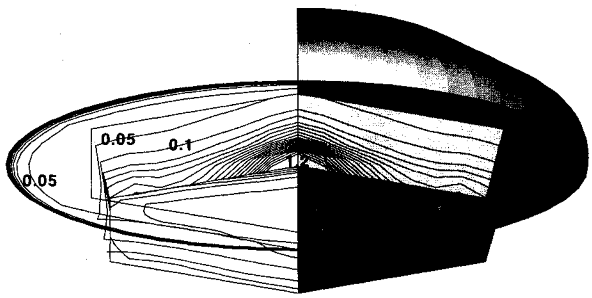

Fig. 16 Side view of heating contours q on AFE carrier for case afe-4 at $\alpha = 22$ deg.

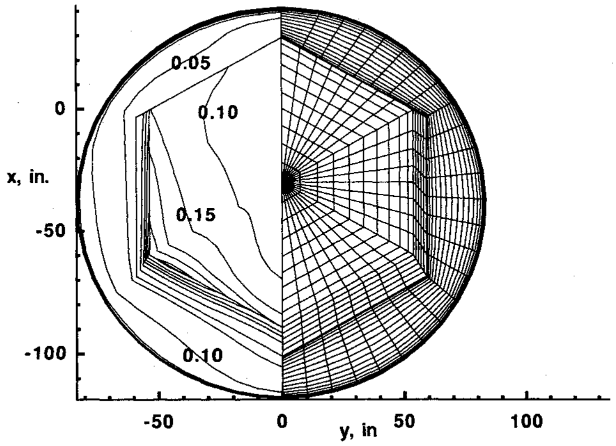

Fig. 17 Bottom view of heating contours q on AFE carrier for case afe-4 at $\alpha = 17$ deg.

The lunar data points in Figs. 10 and 11 include results for both shoulder radii. Differences in shoulder radii and forebody geometry have minor impact on shear-layer deflection angles. The lift-to-drag ratio L/D may also be used to correlate the θ variation; however, the resultant correlation is not any better than that obtained with α. Low density effects at higher altitudes (afe-1) tend to increase shear layer deflection angles by delaying separation off the base plane. (The continuum simulation of this effect at these altitudes is questionable because Knudsen numbers in the near wake exceed the bounds for validity of the constitutive relations for stress, strain, and conduction in the Navier-Stokes equations. Comparison with noncontinuum simulation methods is required to quantify associated errors.) The shear layers in these higher altitude cases are not as clearly defined, though the measurement techniques defined earlier provide an unambiguous measure of θ.

Shear-Layer Impingement and Payload Heating

Shear-layer impingement was calculated for the case afe-4 at $\alpha = 22$ deg. The impingement caused a localized hot spot on the payload/carrier face equal to 1.2 ± 0.3 W/cm^2, approximately equal to 3% of the stagnation heating value. The uncertainty in the value is based on the range of predictions obtained on different grids (19 cells and 57 cells in the zone bounding the impingement point) and two different kinetic models.[6] (The grid density for both the 19 and 57 cell solutions are adequate to resolve gradients at the surface, with cell Reynolds numbers $N_{Re_{\text{cell}}} < 4.0$.) By contrast, for the case afe-4 at $\alpha = 17$ deg, there is no shear layer impingement and the heating at this same location on the carrier face is a factor of 10 smaller (0.3% of the stagnation heating value).

Shear-layer impingement was also calculated for the case afe-1 at $\alpha = 22$ deg and 17 deg. The glancing impingement at $\alpha = 17$ deg is caused primarily by delayed separation off the base plane due to stronger viscous effects. Recall that this

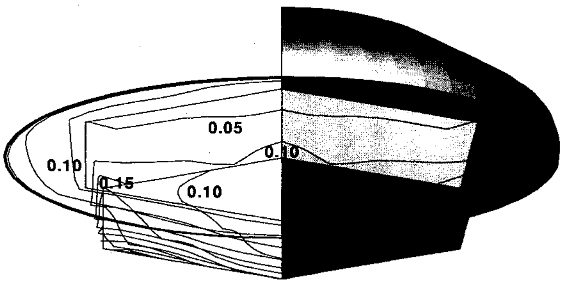

Fig. 18 Side view of heating contours q on AFE carrier for case afe-4 at $\alpha = 17$ deg.

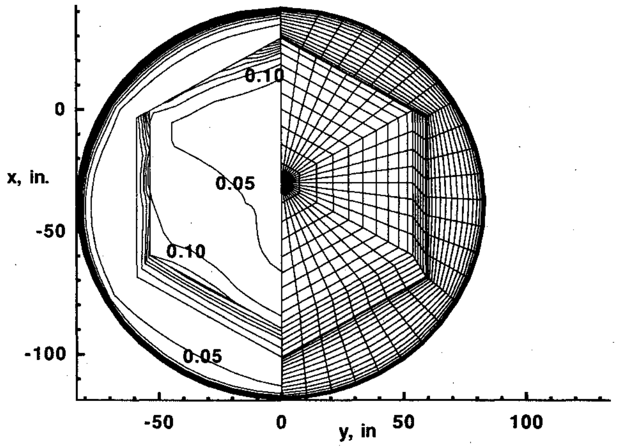

Fig. 19 Bottom view of heating contours q on AFE carrier for case afe-1 at $\alpha = 22$ deg.

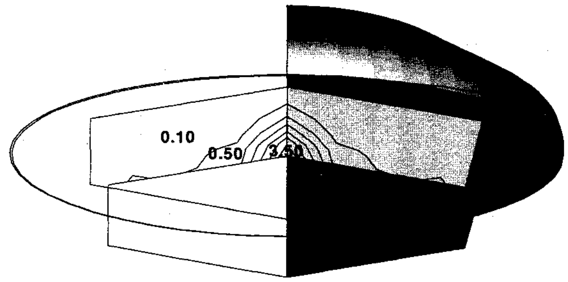

Fig. 20 Side view of heating contours q on AFE carrier for case afe-1 at $\alpha = 22$ deg.

impingement was not observed for the same angle of attack at the lower altitude. Local heating is approximately 3% of stagnation (0.57 W/cm^2) at $\alpha = 17$ deg and approximately 13% of stagnation (3.5 W/cm^2) at $\alpha = 22$ deg with impingement for case afe-1. These calculations indicate that the brake is a less effective shield as altitude increases, and the peak convective heating on the payload near an impingement point may occur earlier in the trajectory than the peak heating on the aerobrake.

For the higher altitude case afe-1, the heating over the base plane of the carrier tends to be a larger percentage of the stagnation value and slightly larger in absolute magnitude than corresponding values on the carrier at the lower altitude case afe-4. However, it should be cautioned that grid resolution on the base plane is marginally adequate to resolve thermal gradients for case afe-1 with cell Reynolds number at the surface $N_{Re_{\text{cell}}} \approx 5$, and is too coarse for case afe-4 with $N_{Re_{\text{cell}}} \approx 17$. A grid refinement study focusing on the resolution over the payload base plane is required. It should be noted that a trend of base heating to stagnation heating ratio increasing with altitude would differ with experimental and flight data in CO$_2$.[20]

The heating contours on the carriers for these cases are presented in Figs. 15–22. The surface mesh is included on the right side of these figures to enhance a sense of perspective and location on the carrier. In flight, there is a large hole in the base of the carrier that holds the engine before it is jettisoned for the aeropass. This hole is covered in the present calculations.

Details of flow in the symmetry plane above the impingement point are presented in Fig. 23. This pressure-streamline plot shows how separation occurs below the corner of the aerobrake and the formation of a shock over the impingement zone on the carrier/payload.

Possible sources of error, particularly for the 87-km afe-1 test case, are discussed below. The heating magnitudes on the

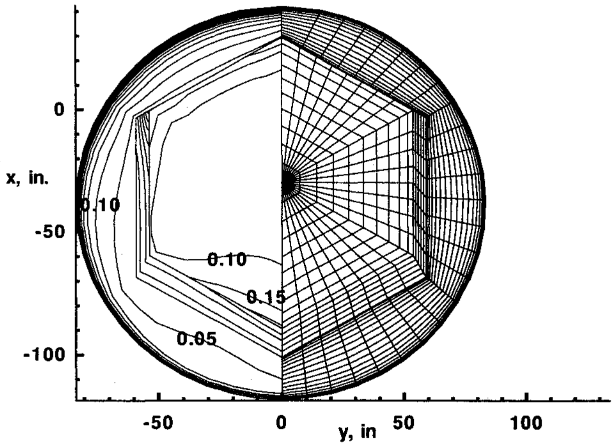

Fig. 21 Bottom view of heating contours q on AFE carrier for case afe-1 at $\alpha = 17$ deg.

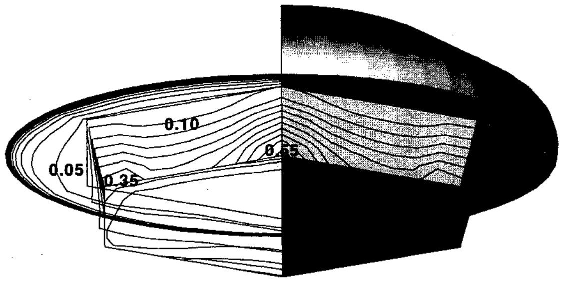

Fig. 22 Side view of heating contours q on AFE carrier for case afe-1 at $\alpha = 17$ deg.

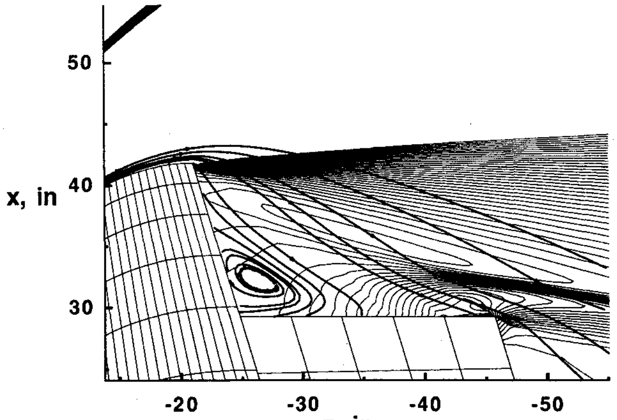

Fig. 23 Detail of pressure contours and streamlines over the impingement point on the AFE carrier for case afe-4 at $\alpha = 22$ deg.

carrier are expected to decrease when temperature and velocity slip are included in the analysis. Also, the effective Knudsen number in the near wake, particularly at the separation point on the shoulder, makes a continuum analysis of this region questionable. Inadequate grid resolution at the shoulder separation point could delay separation and effectively increase the shear-layer deflection angle.[2] A single grid refinement in the afe-4 case showed no evidence that such problems were significant in this study; however, it was not possible to check for absolute grid convergence due to the problem size. Resolution of these issues will require comparisons with AFE flight data, when it becomes available, and with simulations by algorithms more appropriate to rarefied flows. The present results are the best available to work with until three-dimensional, noncontinuum simulation methods can be applied at this altitude.

Concluding Remarks

The numerical simulation of the near-wake flowfield behind three aerobrakes has been implemented for the purpose of providing information to designers concerning the predicted aerothermal environment surrounding a payload behind the aerobrake. Two or three angles of attack have been considered for each configuration. Two altitudes have been included in the AFE computations. Emphasis is placed on understanding the conditions that are likely to cause the shear layer to impinge on the payload.

Flowfield simulation is implemented with Program LAURA, an upwind-biased, point-implicit relaxation algorithm for obtaining the numerical solution to the governing equations for three-dimensional, viscous, hypersonic flows in chemical and thermal nonequilibrium. The analysis includes continuity equations for 11 species, 3 momentum equations, and 2 energy equations describing the conservation of vibrational-electronic and total energies.

Guidelines are provided for generating grids that can be adapted to the developing flow features. In the present study, relatively simple algebraic means have been used to approximately adapt grids to developing flow features. A singularity-free forebody surface mesh has been introduced that avoids numerical problems associated with a coordinate singularity in the stagnation region and provides an enhanced circumferential resolution of flow entering the wake.

A linear relationship between shear-layer deflection angle and angle of attack (or lift-to-drag ratio) has been identified in several ground-based tests. A similar relation appears in the numerical simulations, though there is some evidence that deflection angles may increase somewhat due to the effects of gas chemistry. At higher altitudes (lower Reynolds numbers), the shear-layer separation point from the base plane is delayed, thus increasing the chances of impingement on a payload. Shear-layer impingement can raise local heating levels a factor of 10 higher than levels present without impingement at 75 km in the AFE studies.

References

[1]Freeman, D. C., Powell, R. W., and Braun, R. D., "Manned Mars Aerobrake Vehicle Design Issues," International Aeronautical Federation, IAF Paper 90-197, Oct. 1990.

[2]Gnoffo, P. A., "Code Calibration Program in Support of the Aeroassist Flight Experiment," *Journal of Spacecraft and Rockets,* Vol. 27, No. 2, 1990, pp 131–142.

[3]Jones, J. J., "The Rationale for an Aeroassist Flight Experiment," AIAA Paper 87-1508, June 1987.

[4]Palmer, G., "Enhanced Thermochemical Nonequilibrium Computations of Flow Around the Aeroassist Flight Experiment Vehicle," AIAA Paper 90-1702, June 1990.

[5]Tam, L., and Li, C., "Three Dimensional Thermochemical Nonequilibrium Flow Modeling for Hypersonic Flows," AIAA Paper 89-1860, June 1989.

[6]Gnoffo, P. A., Gupta, R. N., and Shinn, J., "Conservation Equations and Physical Models for Hypersonic Air Flows in Thermal and Chemical Nonequilibrium," NASA TP 2867, Feb. 1989.

[7]Gnoffo, P. A., "Upwind-Biased, Point-Implicit Relaxation Strategies for Viscous, Hypersonic Flows," AIAA Paper 89-1972, June 1989.

[8]Roe, P. L., "Approximate Riemann Solvers, Parameter Vectors, and Difference Schemes," *Journal of Computational Physics,* Vol. 43, No. 2, 1981, pp. 357–372.

[9]Harten, A., "High Resolution Schemes for Hyperbolic Conservation Laws," *Journal of Computational Physics,* Vol. 49, No. 3, 1983, pp. 357–393.

[10]Yee, H. C., "On Symmetric and Upwind TVD Schemes," NASA TM-86842, Sept. 1985.

[11]Yee, H. C., "Numerical Experiments with a Symmetric High-Resolution Shock-Capturing Scheme," NASA TM-88325, June 1986.

[12]Park, C., "Assessment of Two-Temperature Kinetic Model for Ionizing Air," AIAA Paper 87-1574, June 1987.

[13]Stewart, D. A., Leiser, D. B., Kolodziej, P., and Smith, M., "Thermal Response of Integral Multicomponent Composite Thermal Protection Systems," AIAA Paper 85-1056, June 1985.

[14]Grasso, F., and Gnoffo, P. A., "A Numerical Study of Hypersonic Stagnation Heat Transfer Predictions," *Proceedings of the Eighth GAMM Conference on Numerical Methods in Fluid Mechanics,* Notes on Numerical Fluid Mechanics, Vol. 29, Vieweg, Braunschweig, Germany, 1990, pp. 179–188.

[15]Davies, C., and Venkatapathy, E., "A Simplified Self-Adaptive Grid Method, SAGE," NASA TM 102198, Oct. 1989.

[16]Gnoffo, P. A., "A Solution-Adaptive Finite-Volume Alorithm with Application to Problems in Planetary Entry," Ph.D. Dissertation, Princeton Univ., Princeton, NJ, May 1983.

[17]Gnoffo, P. A., "Complete Supersonic Flowfields over Blunt Bodies in a Generalized Orthogonal Coordinate System," NASA TM 81784, March 1980.

[18]Wells, W. L., "Surface Flow and Heating Distributions on a Cylinder in Near Wake of Aeroassist Flight Experiment (AFE) Configuration at Incidence in Mach 10 Air," NASA TP 2954, Jan. 1990.

[19]Hair, L. M., Engel, C. D., Shih, P., Bithell, R., and Bowman, M., "Aerothermal Test Data of Low *L/D* Aerobraking Orbital Transfer Vehicle at Mach 10," RTR 069-1, REMTECH Inc., Huntsville, AL, April 1983.

[20]Schmitt, D. A., "Base Heating on an Aerobraking Orbital Transfer Vehicle," AIAA Paper 83-0408, Jan. 1983.

Ernest V. Zoby
Associate Editor